



# Pt enhanced C–H bond activation for efficient and low-methane-selectivity hydrogenolysis of polyethylene over alloyed RuPt/ZrO<sub>2</sub>

Chengyang Sun<sup>a,1</sup>, Jia Wang<sup>b,1</sup>, Jianjian Wang<sup>c</sup>, Mohsen Shakouri<sup>d</sup>, Bianfang Shi<sup>a</sup>, Xiaohui Liu<sup>a</sup>, Yong Guo<sup>a</sup>, Yongfeng Hu<sup>e</sup>, Xin-Ping Wu<sup>a,b,\*</sup>, Yanqin Wang<sup>a,\*\*</sup>

<sup>a</sup> State Key Laboratory of Green Chemical Engineering and Industrial Catalysis, Research Institute of Industrial Catalysis, School of Chemistry and Molecular Engineering, East China University of Science and Technology, Shanghai 200237, PR China

<sup>b</sup> Centre for Computational Chemistry, School of Chemistry and Molecular Engineering, East China University of Science and Technology, Shanghai 200237, PR China

<sup>c</sup> Multi-Scale Porous Materials Center, Institute of Advanced Interdisciplinary Studies, Chongqing University, Chongqing 400044, PR China

<sup>d</sup> Canadian Light Source Inc., Saskatoon, Saskatchewan S7N 2V3, Canada

<sup>e</sup> Sinopec Shanghai Research Institute of Petrochemical Technology, Shanghai 201208, PR China

## ARTICLE INFO

### Keywords:

Plastic waste  
RuPt alloy catalysts  
Hydrogenolysis  
C–H bond activation  
Internal C–C bond cleavage

## ABSTRACT

Catalytic hydrogenolysis of polyethylene (PE) to liquid alkanes has drawn broad attention due to its high efficiency in the degradation of the largest fraction of plastic wastes. However, the reaction mechanism and the origin of methane selectivity are still ambiguous. Here, we demonstrate that the activation of C–H bonds has a great influence on both the activity and selectivity of polyethylene hydrogenolysis. By introducing Pt with high C–H bond activation efficiency into the monometallic Ru/ZrO<sub>2</sub> catalyst, the alloyed RuPt/ZrO<sub>2</sub> catalyst was successfully synthesized and various characterizations, including HAADF-STEM, EXAFS and H<sub>2</sub>-TPR, elucidated the structure of the RuPt alloy. Compared with the monometallic Ru/ZrO<sub>2</sub> catalyst, the RuPt alloy can enhance the activation of the C–H bonds in the polyethylene chain, thus consequently improving the cleavage of C–C bonds. Surprisingly, the methane selectivity is greatly inhibited on the RuPt alloy. Isotopic TPSR and density functional theory (DFT) calculations reveal that the RuPt alloy has excellent C–H activation capability, the hydrogenolysis rate can be accelerated by promoting the first C–H activation, which is harder on monometallic Ru. Furthermore, the RuPt alloy is more effective in activating internal C–H bonds compared to monometallic Ru, avoiding terminal C–C cleavage generating methane. Additionally, the hydrogenation of intermediates is enhanced on the RuPt alloy, preventing sequential deep dehydrogenation and C–C bond cleavage, ultimately reducing methane formation. This work indicates that the activation of C–H bonds is of great significance for polyethylene hydrogenolysis, which provides a catalyst-designing strategy for polyethylene hydrogenolysis that is more valuable and efficient.

## 1. Introduction

Plastics play an essential role in modern life due to their excellent durability, single-use function and massive-scale manufactures. However, limited by inefficient recycling strategies, approximately 90% of plastic production has been discarded, leading to environmental threats and a severe waste of carbon resources [1]. Therefore, it is urgent to develop efficient and feasible strategies for recycling and upcycling waste plastics. Polyolefins, such as polyethylene (PE) and polypropylene

(PP) constitute more than 60% of global plastic production [2,3], their catalytic depolymerization has drawn great attention worldwide and various catalytic systems have been developed [4–7]. It has been discovered that Ru-based catalysts perform exceptionally well under mild conditions (200–250°C, 2–3 MPa H<sub>2</sub>) [8–12], producing high-value short-chain alkanes such as fuels, waxes and lubricants.

Previous reports have conducted intensive investigations on Ru-based catalysts for PE hydrogenolysis, deepening the understanding of structure-activity relationships and catalytic mechanisms. For example,

\* Corresponding author at: State Key Laboratory of Green Chemical Engineering and Industrial Catalysis, Research Institute of Industrial Catalysis, School of Chemistry and Molecular Engineering, East China University of Science and Technology, Shanghai 200237, PR China.

\*\* Corresponding author.

E-mail addresses: [xpwu@ecust.edu.cn](mailto:xpwu@ecust.edu.cn) (X.-P. Wu), [wangyanqin@ecust.edu.cn](mailto:wangyanqin@ecust.edu.cn) (Y. Wang).

<sup>1</sup> These authors contributed equally to this work.

Chen *et al.* [10] found that the sub-nanometer and cationic Ru species on CeO<sub>2</sub> exhibited remarkable hydrogenolysis activity with low methane selectivity. Jia *et al.* [12] investigated the factors affecting the distribution of hydrogenolysis products on a Ru-based catalyst. They found that higher hydrogen pressure could inhibit the depolymerization reaction. In addition, the depolymerization reaction kinetics were determined by the solvation behavior of PE in different solvents, as confirmed by their molecular dynamics simulation results. Wang and co-workers [13,14] demonstrated that dopant oxides (W, V and Mo) adjacent to Ru on a zirconia support can store and supply additional hydrogen to Ru through reverse hydrogen spillover, which can alleviate hydrogen deficiency and suppress methane formation.

It is important to note that in the hydrogenolysis of alkanes, the first step is the activation and cleavage of the C–H bond, followed by the cleavage of the C–C bond [15–19]. In addition, in other reactions involving alkanes as substrates, such as propane dehydrogenation (PDH) and methane dry reforming (DRM), C–H bond activation is undoubtedly an important step. Despite the remarkable capability of Ru to cleave C–C bonds, its ability to activate C–H bonds has barely been mentioned. With respect to PDH studies, Pt is generally considered to be an efficient active site for PDH due to its affinity for paraffinic C–H bond activation [20–23]. In addition, for the activation of methane, Harrison *et al.* [24] compared the activation energies for the initial C–H bond cleavage of methane over various metals and found that Pt had better activity than those of Ru and Ni.

Taking advantage of Pt for C–H bond activation and Ru for C–C bond cleavage, we synthesized a catalyst with RuPt alloy on ZrO<sub>2</sub> and compared its catalytic performance with monometallic Ru and Pt catalysts. It was found that the enhanced C–H bond activation indeed improved the overall hydrogenolysis reaction. More interestingly, the production of methane was inhibited over the alloyed RuPt/ZrO<sub>2</sub> catalyst compared to the Ru/ZrO<sub>2</sub> catalyst. Comprehensive characterizations were conducted to establish the structure-activity relationships. The unique C–H activation capability of Pt was proved by isotopic temperature-programmed surface reaction (TPSR), and distinguished by model substrates hydrogenation experiments, two pathways generating methane (terminal and sequential cleavage) were both inhibited on RuPt alloy. Furthermore, density functional theory (DFT) calculations of the hydrogenolysis of a model alkane molecule (i.e., n-butane) were conducted to elucidate the intrinsic origin of the selectivity difference between alloyed RuPt and monometallic Ru. The introduction of Pt and the formation of RuPt alloy favor the internal C–H bond activation in the first step. This also accelerates the hydrogenation of intermediates, avoiding sequential dehydrogenation and C–C bond cleavage. As a result, it promotes the hydrogenolysis of PE to alkanes and inhibits the formation of methane.

## 2. Experimental

### 2.1. Materials

Zirconium dioxide (ZrO<sub>2</sub>, 50 nm, 99.99%) and Eicosane (C<sub>20</sub>, 99.0%) were purchased from Shanghai Macklin Biochemical Co., Ltd. RuCl<sub>3</sub>·3 H<sub>2</sub>O and Pt(NO<sub>3</sub>)<sub>2</sub> were purchased from Heraeus Materials Technology Shanghai Co., Ltd. Low-density polyethylene (LDPE, M<sub>w</sub> ~4000) was obtained from Sigma Aldrich. Propane (C<sub>3</sub>H<sub>8</sub>, 99.9%) was obtained from Shanghai Chunyu Special Gas Co., Ltd.

### 2.2. Catalyst preparation

Monometallic Ru/ZrO<sub>2</sub> and Pt/ZrO<sub>2</sub> catalysts were prepared by the incipient wetness impregnation method by using RuCl<sub>3</sub> and Pt(NO<sub>3</sub>)<sub>2</sub> as precursors to achieve a nominal metal loading of 4 wt%, respectively. Alloyed RuPt/ZrO<sub>2</sub> catalyst was prepared by the co-impregnation of RuCl<sub>3</sub> and Pt(NO<sub>3</sub>)<sub>2</sub>, the nominal metal loading of Ru and Pt were 3 and 1 wt%, respectively. These as-prepared samples were dried overnight at

60°C and then calcined at 500°C for 4 h with a heating rate of 5 °C/min. These catalysts were reduced at 400°C (5 °C/min) for 4 h under 10% H<sub>2</sub>/Ar before use.

### 2.3. Catalyst characterization

Powder X-ray diffraction (XRD) patterns were recorded in the  $\theta$ -2 $\theta$  mode on a D8 Focus diffractometer (Cu K $\alpha$  radiation,  $\lambda$  = 1.5406 Å), operated at 40 kV and 40 mA within scattering angles of 10–80°. The specific surface area of the samples was measured on a Micromeritics ASAP 2020 M sorption analyzer at 77 K and calculated with the Brunauer-Emmett-Teller (BET) method. The platinum content was determined by an Agilent 725ES inductively coupled plasma-atomic emission spectrometry (ICP-AES). The ruthenium content was determined by Energy Dispersive Spectroscopy (EDS) using GeminiSEM 500 microscopy. Transmission electron microscopy (TEM) images, high-angle annular dark-field scanning transmission electron microscopy (HAADF-STEM) images, and elemental mappings were recorded on a FEI Talos 200 S microscope under 200 kV.

H<sub>2</sub> temperature-programmed reduction (H<sub>2</sub>-TPR) tests were carried out on a Huasi DAS-7200 automatic chemisorption instrument. In a typical run, 0.1 g of catalyst was put into the quartz tube. Before reduction, the catalyst was degassed and dehydrated at 150°C in Ar. The temperature was controlled from 20 to 600°C at a rate of 10 °C/min under 10% H<sub>2</sub>/Ar atmosphere. X-ray photoelectron spectra (XPS) were recorded on a Thermo Scientific Escalab 250 Xi spectrometer equipped with monochromatic Al K $\alpha$  radiation, and all results were calibrated by a C 1 s peak at 284.6 eV. XAS measurements were conducted at the Canadian Light Source for the Pt L<sub>3</sub>-edge and Ru K-edge on the IDEAS and Bio beamlines, respectively. Catalysts were reduced at 400°C for 4 h under 10% H<sub>2</sub>/Ar mixed gas and transferred in vacuum to avoid oxidation by air. Extended X-ray absorption fine structure (EXAFS) analyses were performed using Athena/Artemis software.

Isotopic TPSR experiments were performed on a temperature-programmed fixed-bed reactor equipped with a mass spectrometer (MS). Typically, 0.1 g of catalyst was loaded in a quartz tube. The sample was pretreated in H<sub>2</sub> (15 mL/min) at 400°C for 2 h with a heating rate of 5 °C/min, then cooled down in Ar until the baseline signal in MS was steady at 35°C. After the pretreatment, D<sub>2</sub> gas (15 mL/min) and CH<sub>4</sub> gas (15 mL/min) were introduced into the reactor and kept for ~15 min at 35°C. Then the heating program started from 35 to 240°C with a ramping rate of 6 °C/min in the same atmosphere and kept for another 20 min at 240°C.

Propane hydrogenolysis tests were conducted in a continuous flow fixed-bed reactor. In a typical procedure, 0.1 g catalyst was loaded in a quartz tube and went through a pretreatment at 400°C for 2 h with H<sub>2</sub>. After that, the hydrogenolysis of propane was conducted at 240°C, 0.1 MPa with different gas flows of C<sub>3</sub>H<sub>8</sub> and H<sub>2</sub> to achieve target propane conversion. The reactor effluent was analyzed by online gas chromatography equipped with a flame ionization detector (FID) and a thermal conductivity detector (TCD).

### 2.4. Catalytic test and product analysis

The catalyst performance was conducted in a stainless-steel autoclave (50 mL) with the desired dosages of substrate and catalyst. Typically, 2 g eicosane or LDPE and 0.1 g catalyst were used. After the autoclave was sealed, the reactor was purged with H<sub>2</sub> three times, then fixed at 3 MPa H<sub>2</sub> at room temperature. Finally, the reactor was maintained at 240°C for a specified time with a magnetic stirring speed of 500 rpm. After the reaction, the reactor was cooled down to room temperature in cooled water. The gas products (C1–C4) were collected in a gas bag and quantitatively analyzed by FID gas chromatograph (KB-Al<sub>2</sub>O<sub>3</sub>/Na<sub>2</sub>SO<sub>4</sub> column). Liquid products (C5–C35) were extracted from the liquid–solid residuals with 5 mL p-xylene and then 400  $\mu$ L of mesitylene was added as the internal standard for analysis. The

quantitative analysis was executed on a GC system (Agilent 7890B) equipped with an HP-5 column and an FID detector. The carbon molar yield ( $Y_i$ ) of the product alkane ( $C_i$ ) with  $i$  carbon atoms was calculated as:

$$Y_i = n_i/n_{\text{initial}}$$

$$n_i = n_x \times i$$

where  $n_x$  is the molar amount of alkane ( $C_i$ ) obtained from the quantitatively analyzed by GC-FID,  $i$  is the number of carbon atoms in alkane ( $C_i$ ),  $n_i$  is the carbon molar amount of alkane ( $C_i$ ) and  $n_{\text{initial}}$  is the carbon molar amount of the initial eicosane or LDPE feedstock.

## 2.5. DFT calculations

Spin-polarized DFT calculations with the Perdew-Burke-Ernzerhof (PBE) functional [25] were performed using the Vienna *Ab initio Simulation Package* (VASP) [26]. The D3 method of Grimme et al. [16] was used to capture the dispersion interactions between the adsorbate and the substrate. The interaction between core and valence electrons was described using the projector augmented wave (PAW) method [27]. A plane-wave kinetic energy cutoff of 500 eV was used for all calculations. Geometry optimizations were finished when the Hellman-Feynman force on each relaxed ion was less than  $0.05 \text{ eV} \cdot \text{\AA}^{-1}$ . The convergence criterion for electronic minimization was  $10^{-6} \text{ eV}$ . The optimized lattice parameters for hexagonal close-packed (hcp) Ru ( $a = b = 2.706 \text{ \AA}$ ,  $c = 4.281 \text{ \AA}$ ), and face-centered cubic (fcc) Pt ( $a = b = c = 3.965 \text{ \AA}$ ) agree well with the experimental values (Ru:  $a = b = 2.706 \text{ \AA}$ ,  $c = 4.282 \text{ \AA}$ ; Pt:  $a = b = c = 3.924 \text{ \AA}$ ) [25,28].

The Pt(111) and Ru(0001) surfaces were modeled with a  $(3 \times 3)$  surface cell, and the surface slab models contain four atom layers. The calculation results indicate that Pt prefers to alloy on the surface of Ru (0001) rather than in the subsurface (see Fig. S12 and Table S7). Therefore, the RuPt surface was constructed by substituting surface Ru atoms with Pt in the Ru(0001) surface slab. The energetically favorable distribution pattern of the RuPt surface alloy is shown in Fig. S13 and Table S8. A large vacuum gap ( $> 15 \text{ \AA}$ ) was applied in the models to eliminate slab-slab interactions. The bottom two atom layers were fixed during geometry optimizations. A gamma-point centered  $2 \times 2 \times 1$   $k$ -

point mesh was used for the Brillouin-zone integrations. The climbing image nudged-elastic band (CI-NEB) algorithm was employed to locate the transition state structures [29]. VESTA was used for visualization [30].

## 3. Results and discussion

### 3.1. Catalytic performance of the RuPt/ZrO<sub>2</sub> catalyst

The promoting effect of Pt in the RuPt/ZrO<sub>2</sub> catalyst was first demonstrated in the hydrogenolysis of C–C bonds in eicosane (C<sub>20</sub>), a model substrate, at 240°C and 3 MPa H<sub>2</sub>. The alloyed RuPt/ZrO<sub>2</sub> catalyst was prepared by the co-impregnation method with a nominal metal loading of 3 wt% Ru and 1 wt% Pt. For comparison purposes, we also prepared monometallic catalysts of Ru/ZrO<sub>2</sub> and Pt/ZrO<sub>2</sub> using the same method. The nominal metal loading for the catalysts was 4 wt%. Fig. 1a–c show the conversions and product yields of the Pt/ZrO<sub>2</sub>, Ru/ZrO<sub>2</sub> and RuPt/ZrO<sub>2</sub> catalysts. It is demonstrated that Pt/ZrO<sub>2</sub> exhibits negligible activity for C<sub>20</sub> hydrogenolysis under the reaction condition (Fig. 1a), consistent with previous studies [9,12]. Ru is widely regarded as an excellent metal for the hydrogenolysis of alkanes. The Ru/ZrO<sub>2</sub> catalyst achieved a C<sub>20</sub> conversion rate of 95.3% in 3 h (Fig. 1b). Using the alloyed RuPt/ZrO<sub>2</sub> catalyst, a conversion rate of 93.9% can be achieved in just 1 h (Fig. 1c). These results indicate that the introduction of Pt into Ru enhances the ability to cleave C–C bonds. Fig. 1d–f show the performance of the Ru/ZrO<sub>2</sub> and RuPt/ZrO<sub>2</sub> catalysts in the hydrogenolysis of polyethylene. The total yield of gas and liquid products over Ru/ZrO<sub>2</sub> is 10.1% (Fig. 1d), which is significantly lower than that of RuPt/ZrO<sub>2</sub> (77.9%, see Fig. 1f) at the same reaction time (8 h). Even with an extension of the reaction time to 16 h over Ru/ZrO<sub>2</sub>, the yield only reached 43.3% (Fig. 1e). The activity tests conducted on PE are consistent with the results obtained for C<sub>20</sub>.

In addition to its high activity in C–C bond cleavage, it is surprising that the RuPt/ZrO<sub>2</sub> catalyst has a much lower methane (C<sub>1</sub>) yield (3.8% in Fig. 1c) compared to the monometallic Ru/ZrO<sub>2</sub> catalyst (11.2% in Fig. 1b) despite similar C<sub>20</sub> conversion. The same trend was also observed for LDPE hydrogenolysis (Figs. 1e and 1f). These results indicated that the generation of methane was greatly inhibited over the alloyed RuPt/ZrO<sub>2</sub> catalyst. It has been reported that methane can be

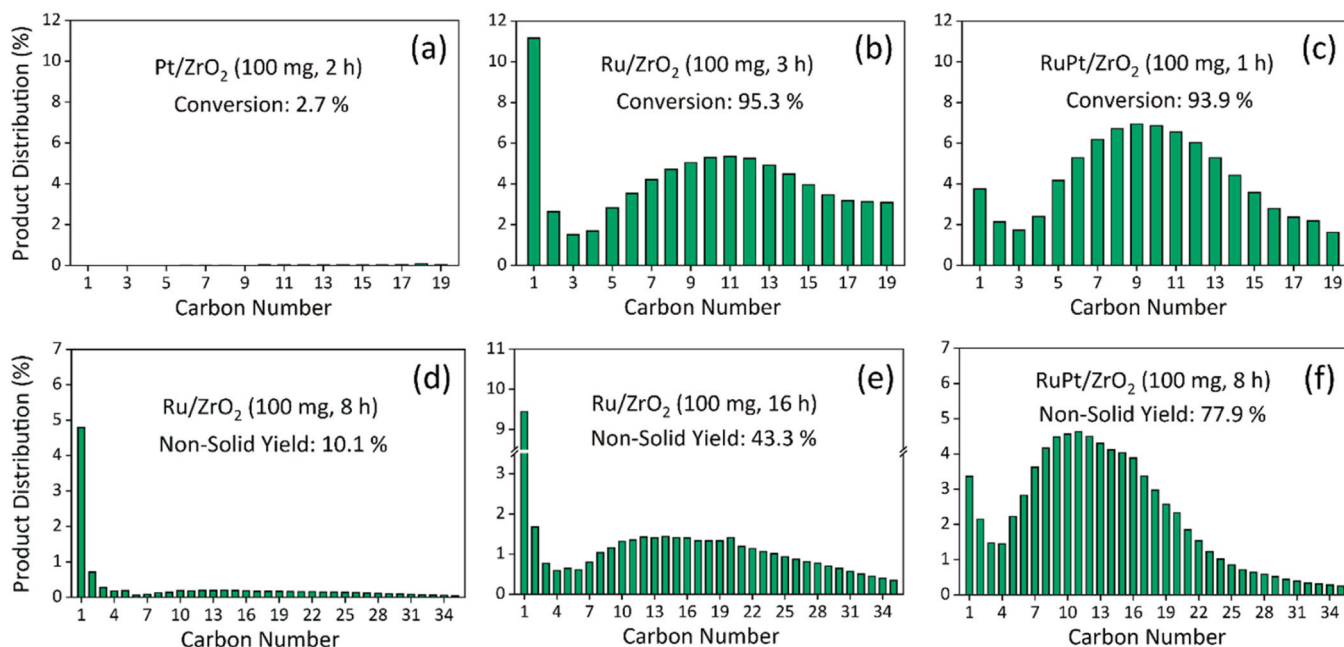


**Fig. 1.** Hydrogenolysis product distribution over various catalysts. (a), (b) and (c) for C<sub>20</sub>; (d), (e) and (f) for LDPE. Reaction condition: 2 g substrate, 100 mg catalysts, 240°C, 3 MPa H<sub>2</sub>.



generated via two pathways: the terminal C–C bond cleavage and the sequential cleavage of alkyl intermediates[14]. Further details will be discussed in the later section. In industrial practice, liquid products (C5–C22) are generally more cost-effective to store, separate and transport than methane and other gas products. Therefore, the higher yield of liquid products from the hydrogenolysis of polyethylene over RuPt/ZrO<sub>2</sub> is of more practical significance.

Based on the comparison of the results presented in Fig. 1, it can be concluded that the introduction of Pt into Ru not only significantly enhances C–C bond cleavage but also reduces the production of methane. Since Pt itself does not have hydrogenolysis activity for alkane under such mild reaction conditions, the catalyst exhibits a synergistic effect between Ru and Pt. To better understand the role of Pt, a control experiment was conducted by physically mixed Ru/ZrO<sub>2</sub> and Pt/ZrO<sub>2</sub>, in which the total amount of metal was the same as that in the alloyed RuPt/ZrO<sub>2</sub> catalyst. The results in Fig. S1 show that the activity of the physically mixed catalyst was much lower than that of RuPt/ZrO<sub>2</sub>, but the same as that of the 0.05 g Ru/ZrO<sub>2</sub> catalyst. This confirms that the physically mixed Pt/ZrO<sub>2</sub> component did not contribute to the reaction, further supporting the synergistic effect of the adjacent Ru–Pt sites. To investigate this effect further, we conducted detailed characterizations of the structure of the alloyed RuPt/ZrO<sub>2</sub> as well as the Ru/ZrO<sub>2</sub> and Pt/ZrO<sub>2</sub> catalysts.

### 3.2. Characterization of the catalysts

The XRD patterns presented in Figs. 2a and 2b show that the monoclinic phase of zirconia (*m*-ZrO<sub>2</sub>) remained after loading and reduction, and the diffraction peaks characteristic of Ru and Pt were observed over monometallic Ru/ZrO<sub>2</sub> and Pt/ZrO<sub>2</sub>, respectively. While using the alloyed RuPt/ZrO<sub>2</sub> catalyst, only diffraction peaks corresponding to Ru were observed, without signals corresponding to Pt, considering Pt content in RuPt/ZrO<sub>2</sub> measured by ICP was only 0.58 wt %, it may not have diffraction in XRD. The TEM images presented in Fig. 2c–e show that the average size of Pt particles in Pt/ZrO<sub>2</sub> is 2.5 nm,

while those in Ru/ZrO<sub>2</sub> and RuPt/ZrO<sub>2</sub> are 13.5 and 12.8 nm, respectively.

Subsequently, RuPt/ZrO<sub>2</sub> was probed using HAADF-STEM and EDX mapping to resolve the fine structures of Ru and Pt on ZrO<sub>2</sub>. Fig. 3a shows the atomic scale image of a RuPt particle. The corresponding element mapping highlights that Ru (Fig. 3e) and Pt (Fig. 3d) formed RuPt alloy with high homogenization, which can be supported by previous works[31–33]. The line profiles in Fig. 3c, which run across the RuPt alloy particle in the direction shown in Fig. 3b, illustrate the close relationship between Ru and Pt. The measured spacing of the lattice in Fig. 3h is 0.216 nm, which can be attributed to the (101) plane of Ru. This crystalline structure was also confirmed in Fig. 2b. It is important to note that the lattice spacing is larger than the standard spacing of Ru (101), which is 0.206 nm. This indicates that Pt has been incorporated into the Ru lattice to form an alloy, resulting in lattice expansion.

The formation of RuPt alloy was further confirmed by EXAFS measurements and H<sub>2</sub>-TPR in Fig. 4. Fig. 4a shows the Pt L<sub>3</sub>-edge FT-EXAFS spectra of Pt/ZrO<sub>2</sub>, RuPt/ZrO<sub>2</sub> and Pt foil. The spectrum of Pt foil exhibits a peak of high intensity at around 2.6 Å associated with Pt–Pt scattering of the first coordination shell. The radial distribution function of the Pt/ZrO<sub>2</sub> catalyst is very similar to that of the Pt reference. However, the radial distance decreases to around 2.4 Å in the alloyed RuPt/ZrO<sub>2</sub> catalyst. This distance is closer to the Ru–Ru scattering path shown in Fig. 4b, indicating a strong contribution of the Ru–Pt scattering path.[34–36] Also, the amplitudes of both catalysts are about half of the Pt foil (Fig. 4a), suggesting the good dispersion of the catalysts (consistent with the XRD, that no Pt feature was detected). This can be regarded as another evidence for the formation of RuPt alloy. Furthermore, the H<sub>2</sub>-TPR profiles shown in Fig. 4c indicate that the reduction temperatures for Ru in Ru/ZrO<sub>2</sub> and Pt in Pt/ZrO<sub>2</sub> are 136 and 97°C, respectively. In comparison, the reduction peak of RuPt/ZrO<sub>2</sub> appeared at 116°C, right between monometallic Ru and Pt. The merging of the two peaks for Ru and Pt can be attributed to the formation of a RuPt alloy. The characterization results strongly suggest the formation of a RuPt alloy on *m*-ZrO<sub>2</sub>. It is speculated that the intermetallic Ru–Pt interface

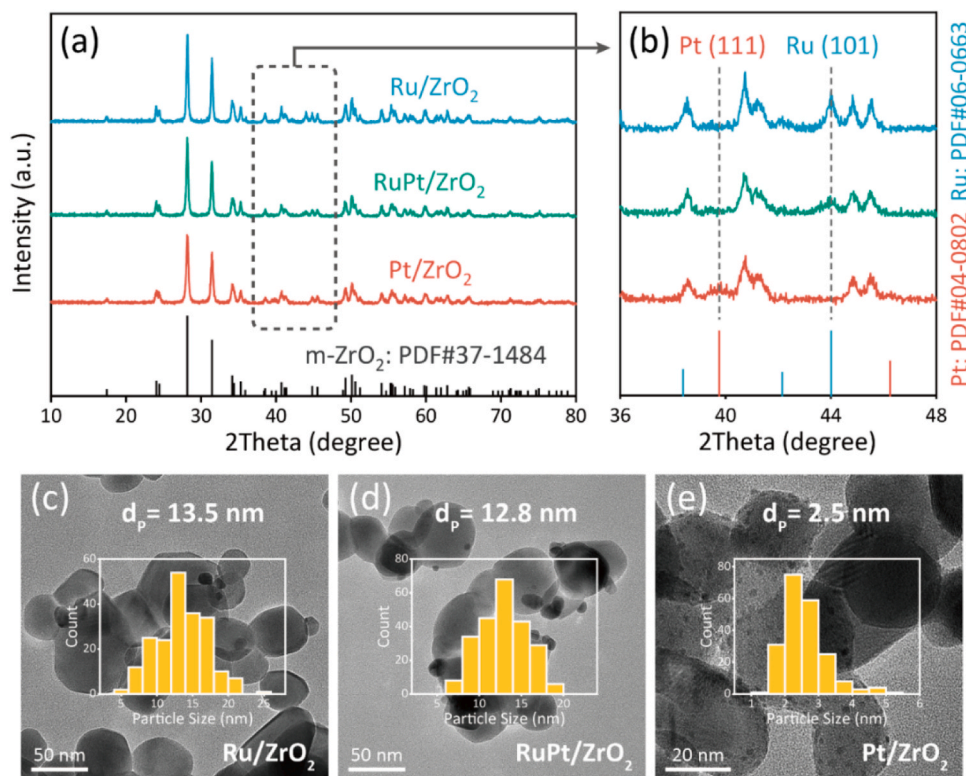
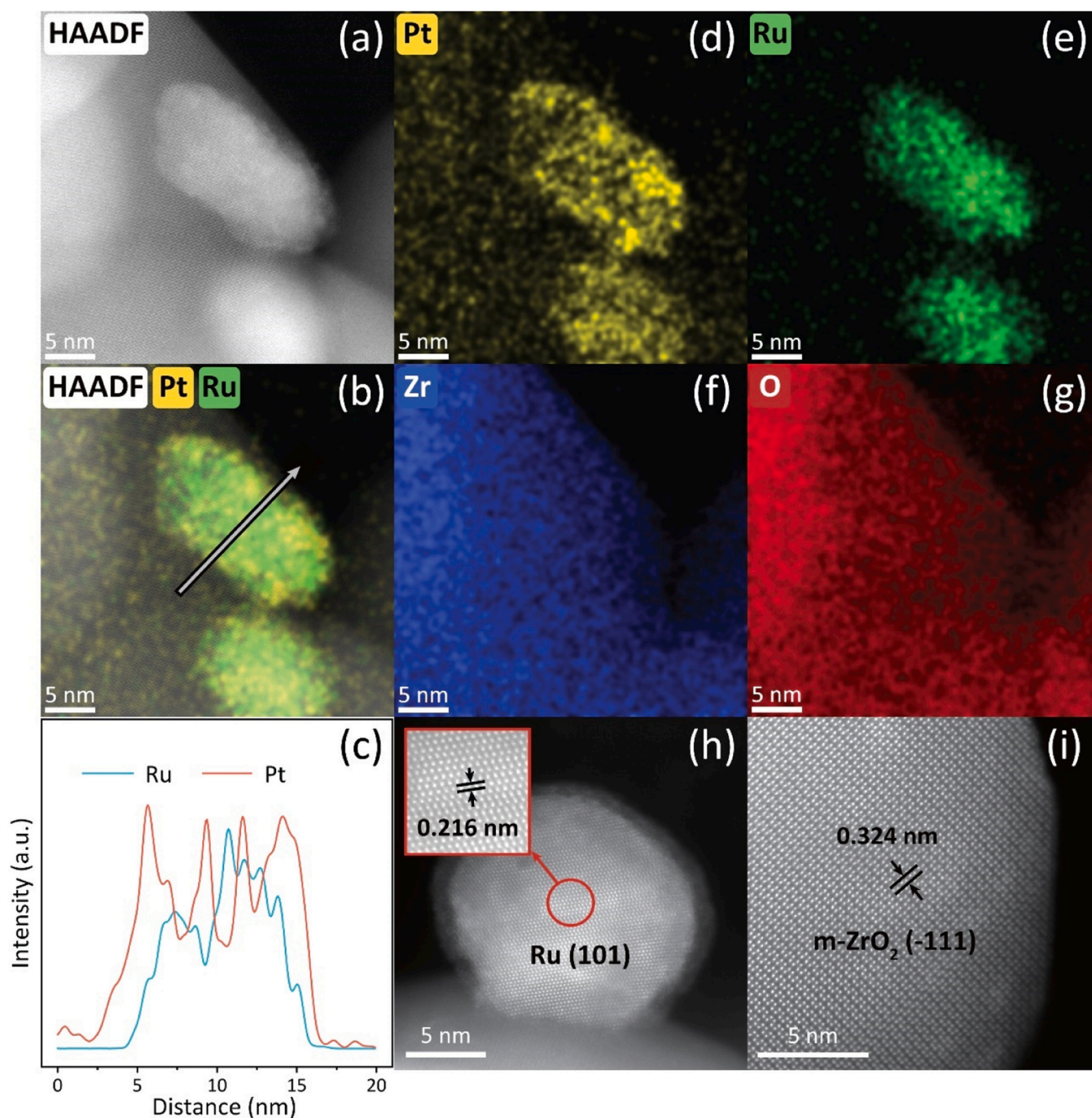


Fig. 2. (a) and (b) XRD patterns of Ru/ZrO<sub>2</sub>, RuPt/ZrO<sub>2</sub> and Pt/ZrO<sub>2</sub>. TEM images and particle size distributions of (c) Ru/ZrO<sub>2</sub>, (d) RuPt/ZrO<sub>2</sub> and (e) Pt/ZrO<sub>2</sub>.



**Fig. 3.** Electron microscopy characterization of the RuPt/ZrO<sub>2</sub> catalyst: (a) HAADF-STEM image of a RuPt/ZrO<sub>2</sub> nanoparticle. (b) Signal overlap of (d) Pt and (e) Ru. (c) Line intensity profiles across RuPt alloy particles in the direction shown in (b). (d–g) EDX elemental maps of Pt (yellow), Ru (green), O (red) and Zr (blue) for the particle in (a). (h) HAADF-STEM image of RuPt alloy particle with (101) lattice plane. (i) HAADF-STEM image of m-ZrO<sub>2</sub> support with (-111) lattice plane.

serves as the intrinsic active site for alkane hydrogenolysis, due to the close proximity of Ru and Pt sites and the observed high activity. The XPS spectra of the three catalysts were recorded and shown in Fig. S3, after the formation of RuPt alloy, the ratio of metallic Ru<sup>0</sup> and Pt<sup>0</sup> became larger compared to monometallic Ru and Pt, indicating a more metallic status of the RuPt alloy.

### 3.3. C–H bond activation

To verify if doping of Pt can facilitate the activation of C–H bonds in alkane, we conducted isotopic TPSR experiments on these three catalysts with methane as a model substrate. Unlike other alkanes with number of

carbon atoms greater than or equal to 2, which would cleave C–C bonds during the heating process, methane only contains four C–H bonds. Therefore, the consumption of D<sub>2</sub> and yield of deuterated products can identify the degree of C–H bond activation. The reactor was loaded with the catalyst and a mixture of CH<sub>4</sub> and D<sub>2</sub> was introduced at 35°C. The temperature was maintained at 35°C for 15 min, followed by an increase to 240°C (hydrogenolysis reaction temperature) at a rate of 6 °C/min. The temperature was then held at 240°C for an additional 20 min. Fig. 5 shows the signals for CH<sub>4</sub>, D<sub>2</sub> and their deuterated products, while the corresponding temperature-programmed profile is illustrated on the top (green line).

During the pretreatment stage at 35°C, the Pt/ZrO<sub>2</sub> catalyst showed



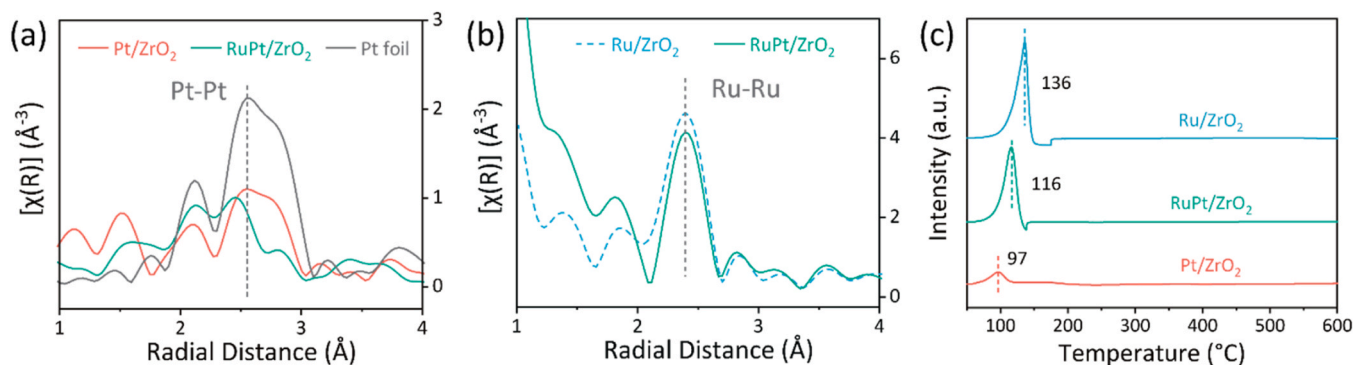


Fig. 4. (a) Pt L<sub>3</sub>-edge FT-EXAFS spectra of Pt/ZrO<sub>2</sub>, RuPt/ZrO<sub>2</sub> and Pt foil. (b) Ru K-edge FT-EXAFS spectra of Ru/ZrO<sub>2</sub> and RuPt/ZrO<sub>2</sub>. (c) H<sub>2</sub>-TPR profiles of Ru/ZrO<sub>2</sub>, RuPt/ZrO<sub>2</sub> and Pt/ZrO<sub>2</sub>.

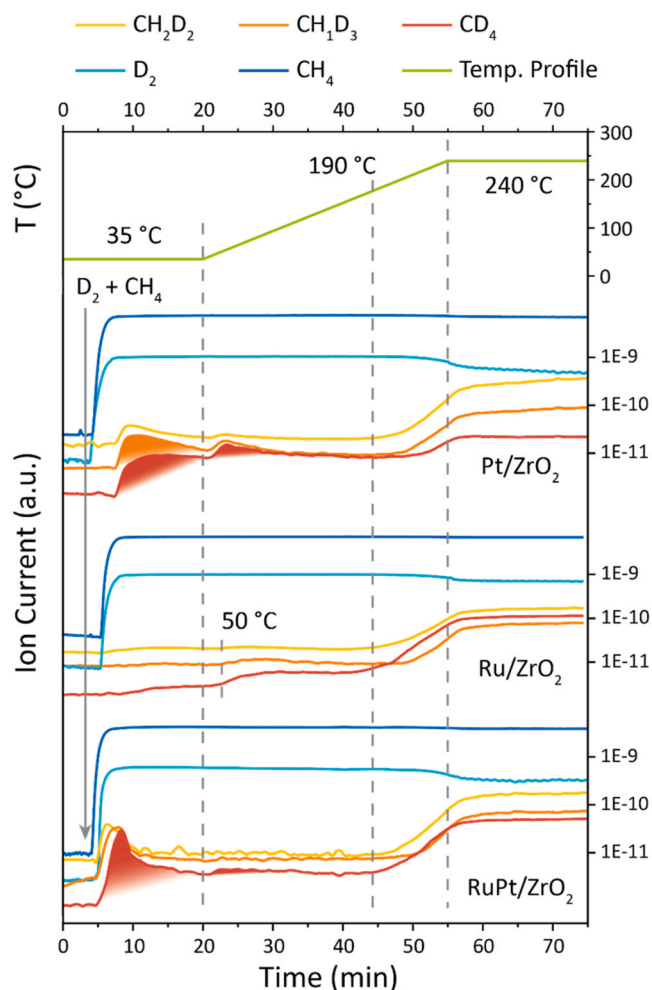


Fig. 5. Isotopic TPSR experiments for Pt/ZrO<sub>2</sub>, RuPt/ZrO<sub>2</sub> and Ru/ZrO<sub>2</sub>.

an increase in signals of CH<sub>2</sub>D<sub>2</sub>, CHD<sub>3</sub> and CD<sub>4</sub> with a delay from the injection of the feed gas. In contrast, no apparent deuterated products of CH<sub>4</sub> were observed over the Ru/ZrO<sub>2</sub> catalyst. These results demonstrate that Pt can dissociate C–H bonds at low temperatures, while Ru cannot. The desorption peaks of CH<sub>2</sub>D<sub>2</sub>, CHD<sub>3</sub> and CD<sub>4</sub> were more pronounced for the alloyed RuPt/ZrO<sub>2</sub> catalyst compared to the monometallic Pt catalyst. Subsequently, deuterated products were observed to desorb over all three catalysts as the temperature was raised. At 50 °C, there was a slight increase in deuterated products over Ru/ZrO<sub>2</sub>, but it was not as noticeable as those observed on Pt and RuPt at 35 °C. Therefore, it is

believed that Ru/ZrO<sub>2</sub> is unable to activate C–H bonds at low temperatures. As the temperature increased, significant signal enhancements of deuterated products were observed at around 190 °C for all three catalysts. At a practical hydrogenolysis temperature of 240 °C, after being kept for 20 min to achieve equilibrium, a noticeable consumption of D<sub>2</sub> was observed.

Furthermore, the consumption of D<sub>2</sub> over each catalyst can be considered as a measure of C–H bond activation. The signal intensity of D<sub>2</sub> was recorded during the two equilibrium stages at 35 and 240 °C, as shown in Fig. 5. Subsequently, we calculated the D<sub>2</sub> consumption during the programmed-temperature rising. Fig. 6 shows that D<sub>2</sub> consumption over Pt (56.3%) was almost twice that of Ru (29.3%). The capability of C–H activation was significantly improved (47.7%) due to the doping of Pt. In addition, the proportion of deuterated products differs among the three catalysts. The Pt/ZrO<sub>2</sub> catalyst produced mainly CH<sub>2</sub>D<sub>2</sub> with a low degree of deuteration, while the Ru/ZrO<sub>2</sub> catalyst had a higher degree of deuteration and nearly equal signal intensities of CH<sub>2</sub>D<sub>2</sub>, CHD<sub>3</sub> and CD<sub>4</sub>. The alloyed RuPt/ZrO<sub>2</sub> catalyst further improved the intensity of CHD<sub>3</sub> and CD<sub>4</sub>. This degree of deuteration can indicate the dehydrogenation behavior in the hydrogenolysis reaction. The Ru site tends to perform deep dehydrogenation when activating alkanes. The formation of a RuPt alloy also exhibits this feature, generating more deep-dehydrogenated intermediates. This will be discussed further in the DFT calculation section. Based on the isotopic TPSR experiment and the catalytic performance analysis, it can be concluded that Pt has a significant ability for C–H bond activation. The formation of a RuPt alloy integrates the unique features of both Ru and Pt, resulting in unique C–C bond cleavage and deep dehydrogenation ability coupled with enhanced C–H activation. The RuPt alloy catalyst exhibits high activity for the hydrogenolysis of alkanes due to a synergistic effect that leads to the rapid formation and subsequent cracking of intermediates.

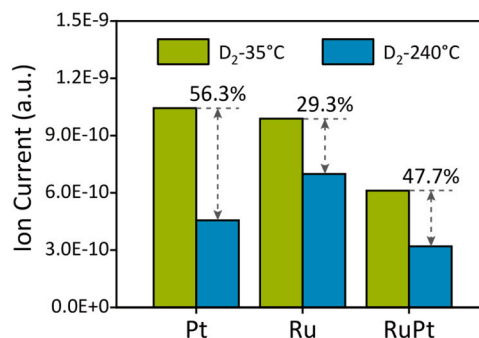


Fig. 6. D<sub>2</sub> intensity at 35 °C and 240 °C recorded in Fig. 5, and calculated D<sub>2</sub> consumption (%) over Pt/ZrO<sub>2</sub>, Ru/ZrO<sub>2</sub> and RuPt/ZrO<sub>2</sub>.

### 3.4. Methane selectivity

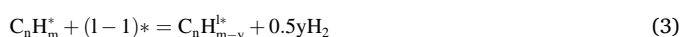
Motivated by the significant difference in the selectivity of methane between Ru/ZrO<sub>2</sub> and RuPt/ZrO<sub>2</sub>, we further explored the mechanism of methane generation. Previous reports [14] indicate that methane can be generated through two pathways: terminal cleavage and sequential cleavage. Taking the cleavage of C<sub>4</sub> as an example, Scheme 1 shows that terminal cleavage can be competitive with internal cleavage, generating C<sub>1</sub>+C<sub>3</sub> and C<sub>2</sub>+C<sub>2</sub>, respectively. After the terminal or internal cleavage, the unhydrogenated alkyl intermediates undergo further cleavage of C–C bonds, known as sequential cleavage, resulting in the conversion of C<sub>4</sub> molecules into methane. This demonstrates that methane can be produced through two distinct mechanisms.

When C<sub>20</sub> was used as a substrate, the terminal C–C cleavage products were C<sub>19</sub> and methane. The yield of methane is contributed from many parts, including terminal or sequential cleavage of all alkanes. Therefore, the yield of C<sub>19</sub> is used as a descriptor for terminal cleavage. Fig. 7a shows that at lower conversion of C<sub>20</sub>, the yield of C<sub>19</sub> over RuPt alloy was only 2.8%, which is half of that over monometallic Ru (7.6%, Fig. 7b). This difference still existed even at higher conversion in Fig. 1 (1.6% for RuPt and 3.1% for Ru). Interestingly, on RuPt/ZrO<sub>2</sub>, the yield of C<sub>19</sub> (terminal cleavage product) was even lower than the yield of C<sub>18</sub> (internal cleavage product), suggesting that the terminal C–C cleavage can be inhibited on RuPt alloy.

Propane was selected as the probe molecule for sequential cleavage because it has only two terminal C–C bonds, which minimize the impact of terminal or internal cleavage selectivity compared to C<sub>3</sub>≥4. In addition, the two C–C bonds enable the occurrence of sequential cleavage shown in Scheme 1, resulting in a higher production of methane (C<sub>1</sub>) compared to ethane (C<sub>2</sub>). The yield ratio of C<sub>1</sub>/C<sub>2</sub> can be used to estimate the tendency of sequential cleavage. In brief, a mixture of H<sub>2</sub> and propane was introduced into the reactor loaded with the catalyst at 240°C, and the conversion of propane was controlled at a similar level for both Ru and RuPt catalysts. Fig. 7c shows that at a conversion rate of 20%, the ratio of C<sub>1</sub>/C<sub>2</sub> was 1.29 for RuPt, while the selectivity of C<sub>1</sub> was significantly higher than that of C<sub>2</sub> on Ru (C<sub>1</sub>/C<sub>2</sub> = 22.6). The results indicate that monometallic Ru has a remarkable ability for sequential dissociation of alkanes, while the formation of RuPt alloy greatly suppresses this process (the second pathway). Surprisingly, the inhibition of RuPt can even occur under higher propane conversion (Fig. 7d). Therefore, it can be concluded that the RuPt alloy strongly inhibits both terminal and sequential cleavage, resulting in low methane selectivity and high liquid production over RuPt/ZrO<sub>2</sub>.

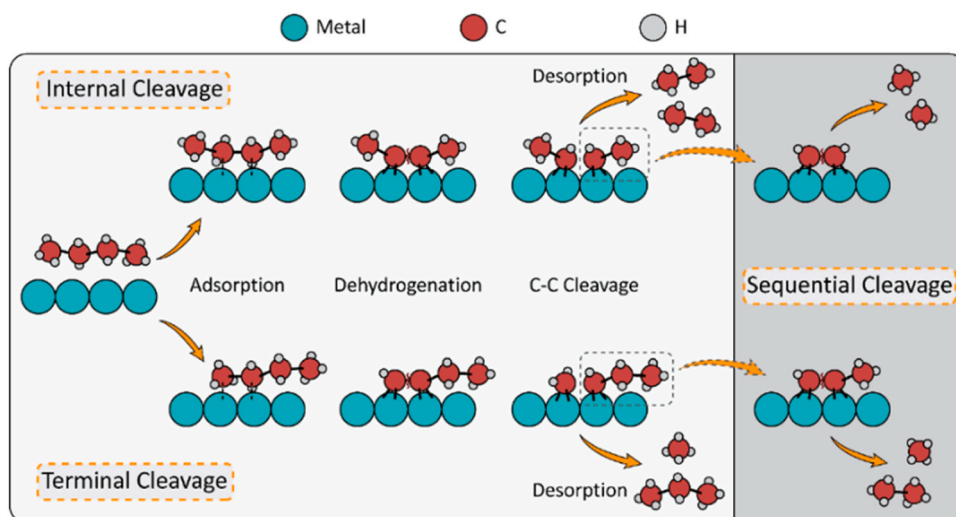
### 3.5. DFT calculations

The hydrogenolysis of alkane is initiated by C–H activation and quasi-equilibrated dehydrogenations. This leads to the progressive replacement of C–H bonds in alkanes by forming C–M (M denotes metal) bonds, thereby weakening the corresponding C–C bond until it is ready for cleavage [15,16,18,19,37,38]. Therefore, the site and depth of CH<sub>x</sub> dehydrogenation in the backbone of alkanes determine the site and rate of C–C bond cleavage [13,17,19,39–42]. DFT calculations were conducted to explore the site preference and reactivity for alkane deep dehydrogenation on the alloy catalyst surface, aiming to offer insight into the mechanism of enhanced selectivity and reactivity for C–C bond cleavage. The Pt(111), Ru(0001) and Pt-alloyed Ru(0001) (denoted as RuPt) surfaces were constructed to model the experimentally synthesized catalysts. It has been reported that the rate constant for cleaving internal C–C bonds is generally independent of chain length and C–C bond location in C<sub>4</sub>+ n-alkanes [43]. Therefore, n-butane is a suitable model compound to represent the experimental substrate and it is the smallest alkane with both internal and terminal C–C bonds. The reaction mechanism for the hydrogenolysis of alkanes on metal surfaces has been proposed previously, as shown in Eqs. 1–5 [17].



It has been demonstrated that the catalysis by metals (Ru, Os, Rh, Ir, Ni, Pd and Pt) in groups 8–10 favors the C–C bond cleavage of the most hydrogen-deficient intermediate, with the formation of three C–M bonds for each C absorbed to the metal surface [15]. Given that the formation of C–M bonds on H-covered catalyst surfaces occurs at the expense of C–H and M–H bonds, both the C–H activation ability and the H affinity of the catalyst are crucial. Therefore, we separately investigated the hydrogenolysis performance and the H affinity features of the catalysts, enabling us to disregard the H coverage effect during the reaction process for the current considerations.

We first examined the H adsorption at various sites on the three catalyst surfaces (Pt/ZrO<sub>2</sub>, Ru/ZrO<sub>2</sub> and RuPt/ZrO<sub>2</sub>). The results are summarized in Fig. S8 and Table S2. The alloyed catalyst showed lower



**Scheme 1.** Three C–C bond cleavage pathways: internal, terminal and sequential C–C cleavage.

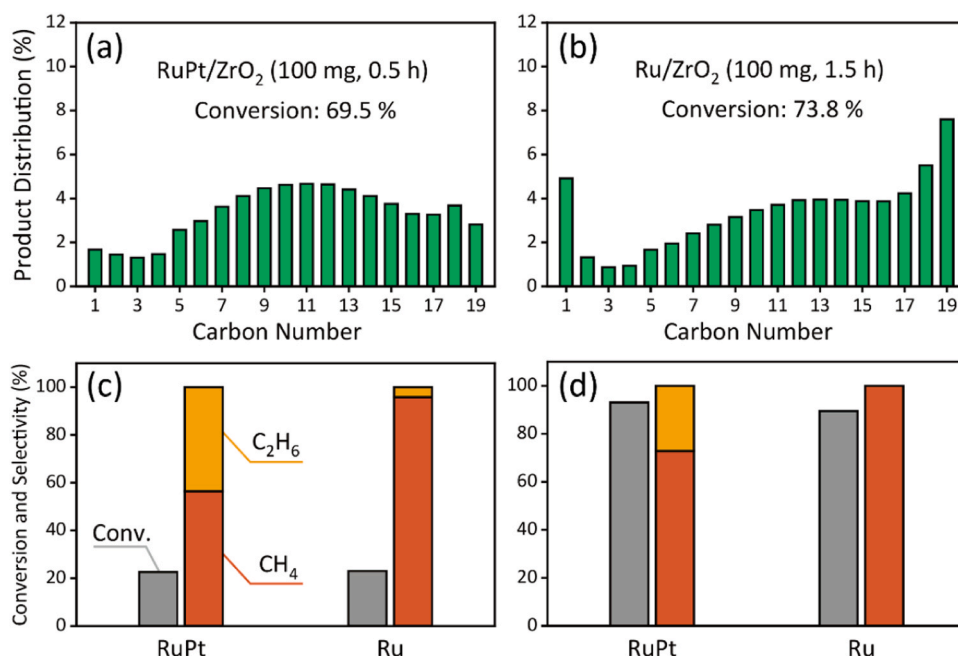
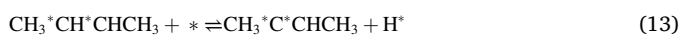
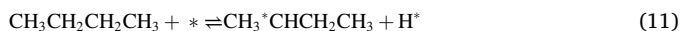
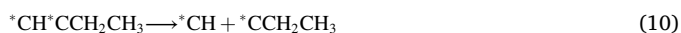
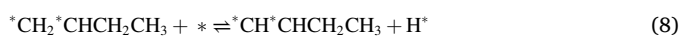
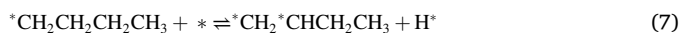
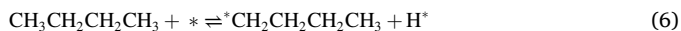


**Fig. 7.** Hydrogenolysis product distribution of C<sub>20</sub> over (a) RuPt/ZrO<sub>2</sub> and (b) Ru/ZrO<sub>2</sub>. Reaction condition: 2 g C<sub>20</sub>, 0.1 g catalyst, 240°C, 3 MPa H<sub>2</sub>. Hydrogenolysis product selectivity of propane over RuPt/ZrO<sub>2</sub> and Ru/ZrO<sub>2</sub> at (c) low and (d) high propane conversion. Reaction condition: 6 mL/min H<sub>2</sub>, 10 mL/min C<sub>3</sub>H<sub>8</sub>, 10 mL/min Ar for (c); 16 mL/min H<sub>2</sub>, 10 mL/min C<sub>3</sub>H<sub>8</sub> for (d), 0.1 g catalyst, 240°C, 0.1 MPa.

H adsorption strength than Ru(0001) and Pt(111), indicating easier H desorption and facilitated H migration on the RuPt surface, which can also contribute to the easier exposure of active sites for butane adsorption and subsequent reactions.

Alkane hydrogenolysis is a highly complex process, we thus focus on two catalytic routes: the formation of the deep dehydrogenation intermediates, C<sub>4</sub>H<sub>6</sub> (e.g., \*CH\*CH<sub>2</sub>CH<sub>3</sub> and CH<sub>3</sub>\*C\*CH<sub>3</sub>), and their cleavage at the terminal (elementary steps as shown in Eqs. 6–10) or internal C–C sites (elementary steps as shown in Eqs. 11–15).



The calculated structures and energy profiles illustrating the performance of hydrogenolysis on the three model catalysts are shown in Fig. S9 and S10, along with corresponding data in Tables S5 and S6. Dehydrogenation is generally unfavorable on Pt(111), except for the first dehydrogenation step, the following dehydrogenation steps on Pt(111) are endothermic by 0.10 ~ 0.68 eV, with energy barriers increasing from 0.72 to 1.28 eV, which is in consistent with the results draw from Fig. 5. It can be expected that the hindered deep hydrogenation process poses a challenge for Pt(111) in alkane hydrogenolysis.

This can explain the minimal conversion of C<sub>20</sub> on the Pt/ZrO<sub>2</sub> catalyst observed experimentally. By comparing the hydrogenolysis energetics of Ru(0001) and RuPt, we found that the introduction of Pt on Ru(0001) led to an increase in the selectivity of the internal C–C bond cleavage.

The difference between terminal and internal C–C bond cleavage in butane hydrogenolysis originates from the first C–H bond activation. Terminal C–C bond cleavage initiates from the dehydrogenation of the terminal methyl, while internal C–C bond cleavage initiates from the dehydrogenation of the internal methylene. Therefore, the reaction energy and energy barrier for the first dehydrogenation step can serve as descriptors for the site selectivity of C–C bond cleavage in alkanes. The first C–H activation at two different sites on the three model catalysts are calculated (Fig. 8). On Ru(0001), the terminal cleavage pathway is dominant due to its lower first C–H activation energy of 0.80 eV compared to the internal cleavage pathway, which has a corresponding activation energy of 1.35 eV. Therefore, it can be expected that light alkane products (e.g., CH<sub>4</sub>) can be extensively generated on Ru(0001), which is consistent with the experimental results. On the RuPt alloy surface, however, the internal pathway with a first C–H activation energy of 0.89 eV is more favorable than the terminal pathway with a corresponding activation energy of 1.06 eV. This results in a reversal of the two competitive pathways, as compared to Ru(0001), leading to an enhanced selectivity of internal C–C bond cleavage and the inhibition of methane formation.

As we mentioned in Scheme 1, the hydrocarbon species formed after C–C bond cleavage can undergo further reactions including (i) hydrogenation to produce the corresponding alkanes and (ii) further hydrogenolysis that may contribute to undesired light alkane products (Scheme 1). The hydrocarbon species, exemplified by M<sub>3</sub>–C<sub>4</sub>H<sub>7</sub>\*, following alkane hydrogenolysis through either terminal or internal C–C bond cleavage, would undergo hydrogenation on the surfaces. This process continues until the species is ready for subsequent hydrogenation or dehydrogenation, illustrated by \*C<sub>4</sub>H<sub>9</sub> in this instance (Fig. S11). Thus, the hydrogenation and dehydrogenation of \*C<sub>4</sub>H<sub>9</sub> were selected as prototype reactions to study the selectivity of the two pathways on the Ru(0001) and RuPt surfaces, and the activation energy results are summarized in Table 1. Encouragingly, \*C<sub>4</sub>H<sub>9</sub> dehydrogenation is



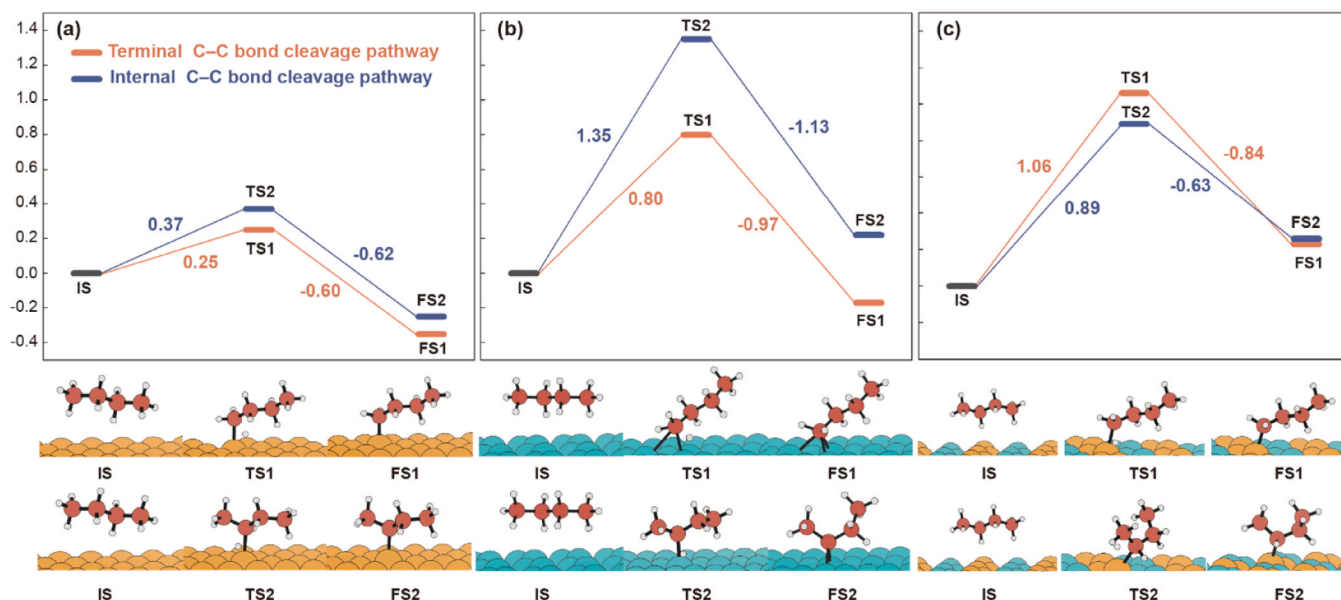


**Fig. 8.** Calculated energy profiles for the first C–H bond activation of butane on (a) Pt(111), (b) Ru(0001) and (c) RuPt alloy surfaces. The corresponding structures are given below; Pt, Ru, C and H atoms are in orange, green, red and gray, respectively.

**Table 1**

Calculated activation energies for the hydrogenation and dehydrogenation of  $^*C_4H_9$  on the Ru(0001) and RuPt surfaces and the activation energy differences.

	hydrogenation	dehydrogenation	difference <sup>a</sup>
Ru(0001)	0.97	0.18	0.79
RuPt	0.84	0.52	0.32

<sup>a</sup> The activation energy of  $^*C_4H_9$  hydrogenation minus the activation energy of  $^*C_4H_9$  dehydrogenation.

significantly hindered, while hydrogenation becomes easier on the RuPt surface compared to the Ru(0001) surface. As a result, the pure Ru catalyst produces more light alkane products compared to the alloy catalyst, which is in accordance with the experimental results shown in Fig. 7.

#### 4. Conclusions

A unique synergistic effect between Ru and Pt was observed in the hydrogenolysis of PE on RuPt/ZrO<sub>2</sub>. The alloy structure was confirmed by HAADF-STEM, EXAFS and H<sub>2</sub>-TPR. The alkane hydrogenolysis efficiency of RuPt alloy was promoted by the excellent C–H bond activation ability of Pt, as demonstrated by catalytic tests, isotopic TPSR and DFT calculations. The study also intensively investigated and clarified the inhibited methane selectivity of RuPt alloy. On RuPt alloy, the activation of the first C–H bond at the internal of the backbone is more favorable than the terminal one. Therefore, subsequent C–C bonds prefer to be cleaved at the internal position. This trend is opposite on Ru. Furthermore, the introduction of Pt can accelerate the hydrogenation of intermediates, thus inhibiting the sequential cleavage. The excellent selectivity of RuPt alloy is still due to the unique C–H activation ability of Pt. The intrinsic reaction mechanism was elucidated explicitly through experimental characterizations and DFT calculations, highlighting the significance of C–H bond activation. This work presents a novel approach to designing PE hydrogenolysis catalysts.

#### CRediT authorship contribution statement

**Chengyang Sun:** Writing – original draft, Investigation, Data curation. **Jianjian Wang:** Methodology, Data curation. **Jia Wang:** Writing –

original draft, Validation, Methodology, Data curation. **Xiaohui Liu:** Methodology, Validation. **Mohsen Shakouri:** Data curation, Investigation. **Yongfeng Hu:** Writing – review & editing, Formal analysis, Validation. **Yong Guo:** Formal analysis, Investigation. **Xin-Ping Wu:** Writing – review & editing, Supervision, Formal analysis. **Yanqin Wang:** Writing – review & editing, Supervision, Investigation, Conceptualization. **Bianfang Shi:** Investigation.

#### Declaration of Competing Interest

The authors declare no competing interests.

#### Data Availability

Data will be made available on request.

#### Acknowledgements

The authors thank the financial supports by the National Key Research and Development Program of China (2022YFA1504903, 2022YFA1504904), the National Natural Science Foundation of China (92145302), the Canada Foundation for Innovation (CFI) and the University of Saskatchewan.

#### Appendix A. Supporting information

Supplementary data associated with this article can be found in the online version at doi:10.1016/j.apcatb.2024.124046.

#### References

- [1] A.J. Martin, C. Mondelli, S.D. Jaydev, J. Perez-Ramirez, Catalytic processing of plastic waste on the rise, *Chem* 7 (2021) 1487–1533.
- [2] E. Butler, G. Devlin, K. McDonnell, Waste polyolefins to liquid fuels via pyrolysis: review of commercial state-of-the-art and recent laboratory research, *Waste Biomass.-. Valoriz.* 2 (2011) 227–255.
- [3] R. Geyer, J.R. Jambeck, K.L. Law, Production, use, and fate of all plastics ever made, *Sci. Adv.* 3 (2017) e1700782.
- [4] A. Tennakoon, X. Wu, A.L. Paterson, S. Patnaik, Y.C. Pei, A.M. LaPointe, S. C. Ammal, R.A. Hackler, A. Heyden, I.I. Slowing, G.W. Coates, M. Delferro, B. Peters, W.Y. Huang, A.D. Sadow, F.A. Perras, Catalytic upcycling of high-density polyethylene via a processive mechanism, *Nat. Catal.* 3 (2020) 893–901.

- [5] S. Liu, P.A. Kots, B.C. Vance, A. Danielson, D.G. Vlachos, Plastic waste to fuels by hydrocracking at mild conditions, *Sci. Adv.* 7 (2021) eabf8283.
- [6] F. Zhang, M. Zeng, R.D. Yappert, J. Sun, Y.H. Lee, A.M. LaPointe, B. Peters, M. M. Abu-Omar, S.L. Scott, Polyethylene upcycling to long-chain alkylaromatics by tandem hydrogenolysis/aromatization, *Science* 370 (2020) 437–441.
- [7] X. Jia, C. Qin, T. Friedberger, Z. Guan, Z. Huang, Efficient and selective degradation of polyethylenes into liquid fuels and waxes under mild conditions, *Sci. Adv.* 2 (2016) e1501591.
- [8] P.A. Kots, S.B. Liu, B.C. Vance, C. Wang, J.D. Sheehan, D.G. Vlachos, Polypropylene plastic waste conversion to lubricants over Ru/TiO<sub>2</sub> Catalysts, *ACS Catal.* 11 (2021) 8104–8115.
- [9] Y. Nakaji, M. Tamura, S. Miyaoka, S. Kumagai, M. Tanji, Y. Nakagawa, T. Yoshioka, K. Tomishige, Low-temperature catalytic upgrading of waste polyolefinic plastics into liquid fuels and waxes, *Appl. Catal. B: Environ.* 285 (2021) 119805.
- [10] L. Chen, L.C. Meyer, L. Kovarik, D. Meira, X.I. Pereira-Hernandez, H. Shi, K. Khivantsev, O.Y. Gutiérrez, J. Szanyi, Disordered, sub-nanometer Ru structures on CeO<sub>2</sub> are highly efficient and selective catalysts in polymer upcycling by hydrogenolysis, *ACS Catal.* (2022) 4618–4627.
- [11] J.E. Rorrer, G.T. Beckham, Y. Roman-Leshkov, Conversion of polyolefin waste to liquid alkanes with Ru-based catalysts under mild conditions, *JACS Au* 1 (2021) 8–12.
- [12] C. Jia, S. Xie, W. Zhang, N.N. Intan, J. Sampath, J. Pfandtner, H. Lin, Deconstruction of high-density polyethylene into liquid hydrocarbon fuels and lubricants by hydrogenolysis over Ru catalyst, *Chem. Catal.* 1 (2021) 437–455.
- [13] C. Wang, T. Xie, P.A. Kots, B.C. Vance, K. Yu, P. Kumar, J. Fu, S. Liu, G. Tsilomelekis, E.A. Stach, W. Zheng, D.G. Vlachos, Polyethylene hydrogenolysis at mild conditions over ruthenium on tungstated zirconia, *JACS Au* 1 (2021) 1422–1434.
- [14] C. Wang, K. Yu, B. Sheludko, T. Xie, P.A. Kots, B.C. Vance, P. Kumar, E.A. Stach, W. Zheng, D.G. Vlachos, A general strategy and a consolidated mechanism for low-methane hydrogenolysis of polyethylene over ruthenium, *Appl. Catal. B: Environ.* 319 (2022) 121899.
- [15] A. Almithn, D. Hibbitts, Comparing rate and mechanism of ethane hydrogenolysis on transition-metal catalysts, *J. Phys. Chem. C* 123 (2019) 5421–5432.
- [16] D.W. Flaherty, D.D. Hibbitts, E.I. Gürbüz, E. Iglesia, Theoretical and kinetic assessment of the mechanism of ethane hydrogenolysis on metal surfaces saturated with chemisorbed hydrogen, *J. Catal.* 311 (2014) 350–356.
- [17] D.D. Hibbitts, D.W. Flaherty, E. Iglesia, Effects of Chain Length on the Mechanism and Rates of Metal-Catalyzed Hydrogenolysis of n-Alkanes, *The, J. Phys. Chem. C* 120 (2016) 8125–8138.
- [18] D.D. Hibbitts, D.W. Flaherty, E. Iglesia, Role of branching on the rate and mechanism of C–C cleavage in alkanes on metal surfaces, *ACS Catal.* 6 (2016) 469–482.
- [19] D.W. Flaherty, D.D. Hibbitts, E. Iglesia, Metal-catalyzed C–C bond cleavage in alkanes: effects of methyl substitution on transition-state structures and stability, *J. Am. Chem. Soc.* 136 (2014) 9664–9676.
- [20] S. Chen, X. Chang, G. Sun, T. Zhang, Y. Xu, Y. Wang, C. Pei, J. Gong, Propane dehydrogenation: catalyst development, new chemistry, and emerging technologies, *Chem. Soc. Rev.* 50 (2021) 3315–3354.
- [21] J.J.H.B. Sattler, J. Ruiz-Martinez, E. Santillan-Jimenez, B.M. Weckhuysen, Catalytic dehydrogenation of light alkanes on metals and metal oxides, *Chem. Rev.* 114 (2014) 10613–10653.
- [22] H.N. Pham, J.J.H.B. Sattler, B.M. Weckhuysen, A.K. Datye, Role of Sn in the regeneration of Pt/ $\gamma$ -Al<sub>2</sub>O<sub>3</sub> light alkane dehydrogenation catalysts, *ACS Catal.* 6 (2016) 2257–2264.
- [23] C. Fricke, B. Rajbanshi, E.A. Walker, G. Terejanu, A. Heyden, Propane dehydrogenation on platinum catalysts: identifying the active sites through bayesian analysis, *ACS Catal.* 12 (2022) 2487–2498.
- [24] H.L. Abbott, I. Harrison, Methane dissociative chemisorption on Ru(0001) and comparison to metal nanocatalysts, *J. Catal.* 254 (2008) 27–38.
- [25] J.P. Perdew, K. Burke, M. Ernzerhof, Generalized gradient approximation made simple, *Phys. Rev. Lett.* 77 (1996) 3865–3868.
- [26] E. Araujo-Lopez, B.D. Vandegehuchte, D. Curulla-Ferré, D.I. Sharapa, F. Studt, Trends in the activation of light alkanes on transition-metal surfaces, *J. Phys. Chem. C* 124 (2020) 27503–27510.
- [27] W. Tang, E. Sanville, G. Henkelman, A grid-based Bader analysis algorithm without lattice bias, *J. Phys. Condens Matter* 21 (2009) 084204.
- [28] G. Kresse, J. Hafner, Ab initio molecular-dynamics simulation of the liquid-metal–amorphous-semiconductor transition in germanium, *Phys. Rev. B* 49 (1994) 14251–14269.
- [29] S. Grimme, J. Antony, S. Ehrlich, H. Krieg, A consistent and accurate ab initio parametrization of density functional dispersion correction (DFT-D) for the 94 elements H–Pu, *The, J. Chem. Phys.* 132 (2010) 154104.
- [30] P.E. Blöchl, Projector augmented-wave method, *Phys. Rev. B* 50 (1994) 17953–17979.
- [31] J. Lee, C. Yeon, J. Oh, G. Han, J. Do Yoo, H.J. Yun, C.-W. Lee, K.T. Lee, J. Bae, Highly active and stable catalyst with exsolved PtRu alloy nanoparticles for hydrogen production via commercial diesel reforming, *Appl. Catal. B: Environ.* (2022) 121645.
- [32] C. Li, L. Zhang, Y. Zhang, Y. Zhou, J. Sun, X. Ouyang, X. Wang, J. Zhu, Y. Fu, PtRu alloy nanoparticles embedded on C<sub>2</sub>N nanosheets for efficient hydrogen evolution reaction in both acidic and alkaline solutions, *Chem. Eng. J.* 428 (2022) 131085.
- [33] J. Teddy, A. Falqui, A. Corrias, D. Carta, P. Lecante, I. Gerber, P. Serp, Influence of particles alloying on the performances of Pt–Ru/CNT catalysts for selective hydrogenation, *J. Catal.* 278 (2011) 59–70.
- [34] L.M.N.C. Alves, M.P. Almeida, M. Ayala, C.D. Watson, G. Jacobs, R.C. Rabelo-Neto, F.B. Noronha, L.V. Mattos, CO<sub>2</sub> methanation over metal catalysts supported on ZrO<sub>2</sub>: effect of the nature of the metallic phase on catalytic performance, *Chem. Eng. Sci.* 239 (2021) 116604.
- [35] S. Matsuda, S. Masuda, S. Takano, N. Ichikuni, T. Tsukuda, Synergistic effect in Ir- or Pt-doped Ru nanoparticles: catalytic hydrogenation of carbonyl compounds under ambient temperature and H<sub>2</sub> pressure, *ACS Catal.* 11 (2021) 10502–10507.
- [36] L.G. Cesar, C. Yang, Z. Lu, Y. Ren, G. Zhang, J.T. Miller, Identification of a Pt<sub>3</sub>Co surface intermetallic alloy in Pt–Co propane dehydrogenation catalysts, *ACS Catal.* 9 (2019) 5231–5244.
- [37] F. Locatelli, J.-P. Candy, B. Didillon, G.P. Nicolai, D. Uzio, J.-M. Basset, Hydrogenolysis of Cyclohexane over Ir/SiO<sub>2</sub> Catalyst: a mechanistic study of carbon–carbon bond cleavage on metallic surfaces, *J. Am. Chem. Soc.* 123 (2001) 1658–1663.
- [38] A. Almithn, D. Hibbitts, Effects of catalyst model and high adsorbate coverages in ab initio studies of alkane hydrogenolysis, *ACS Catal.* 8 (2018) 6375–6387.
- [39] R.H. Crabtree, R.P. Dion, Selective alkane C–C bond cleavage via prior dehydrogenation by a transition metal complex, *J. Chem. Soc., Chem. Commun.* (1984) 1260–1261.
- [40] G. Celik, R.M. Kennedy, R.A. Hackler, M. Ferrandon, A. Tennakoon, S. Patnaik, A. M. LaPointe, S.C. Ammal, A. Heyden, F.A. Perras, M. Pruski, S.L. Scott, K. R. Poeppelmeier, A.D. Sadow, M. Delferro, Upcycling single-use polyethylene into high-quality liquid products, *ACS Cent. Sci.* 5 (2019) 1795–1803.
- [41] R. Wu, K.R. Wiegand, L. Wang, Impact of the degree of dehydrogenation in ethanol C–C bond cleavage on Ir(100), *J. Chem. Phys.* 154 (2021) 054705.
- [42] P.A. Kots, T. Xie, B.C. Vance, C.M. Quinn, M.D. de Mello, J.A. Boscoboinik, C. Wang, P. Kumar, E.A. Stach, N.S. Marinkovic, L. Ma, S.N. Ehrlich, D.G. Vlachos, Electronic modulation of metal-support interactions improves polypropylene hydrogenolysis over ruthenium catalysts, *Nature, Communications* 13 (2022) 5186.
- [43] D.W. Flaherty, E. Iglesia, Transition-State enthalpy and entropy effects on reactivity and selectivity in hydrogenolysis of n-alkanes, *J. Am. Chem. Soc.* 135 (2013) 18586–18599.